Springer Series in Materials Science 173

Helmut Sitter
Claudia Draxl
Michael Ramsey *Editors*

Small Organic Molecules on Surfaces

Fundamentals and Applications

Springer

Springer Series in Materials Science

Volume 173

For further volumes:
www.springer.com/series/856

The Springer Series in Materials Science covers the complete spectrum of materials physics, including fundamental principles, physical properties, materials theory and design. Recognizing the increasing importance of materials science in future device technologies, the book titles in this series reflect the state-of-the-art in understanding and controlling the structure and properties of all important classes of materials.

Helmut Sitter • Claudia Draxl • Michael Ramsey
Editors

Small Organic Molecules on Surfaces

Fundamentals and Applications

Springer

Editors
Helmut Sitter
Semiconductor- and Solid State Physics
Johannes Kepler University Linz
Linz, Austria

Claudia Draxl
Physics Department
Humboldt Universität zu Berlin
Berlin, Germany

Michael Ramsey
Surface and Interface Physics
Institute of Physics
Karl-Franzens University Graz
Graz, Austria

ISSN 0933-033X Springer Series in Materials Science
ISBN 978-3-642-33847-2 ISBN 978-3-642-33848-9 (eBook)
DOI 10.1007/978-3-642-33848-9
Springer Heidelberg New York Dordrecht London

Library of Congress Control Number: 2013931979

Printed on acid-free paper

Springer is part of Springer Science+Business Media (www.springer.com)

Preface

There is an enormous world-wide effort in basic scientific research as well as in industrial development in the area of organic electronics. It is becoming increasingly clear that if devices based on organic materials are ever going to have a significant relevance beyond being a cheap replacement for inorganic semiconductors, one will need to understand interface formation, film growth, and functionality. Control of these aspects will allow the realisation of totally new device concepts exploiting the enormous flexibility inherent in organic chemistry. In the field of device-relevant semiconducting organic materials one finds many parallels with that of inorganic semiconductors. However, the versatility of organic molecules comes at the cost of higher materials complexity. This rules out the simple transfer of concepts established from inorganic semiconductor research, and makes work on organic semiconductors particularly challenging.

World-wide, investigations into organic thin films can be partitioned into three areas of focus with different aims and a mix of applied versus basic research: (1) the development and production of devices, (2) thin film characterisation, and, more recently, with the recognition of the importance of molecular level control (3) surface and interface science. As shown in this volume, linking these branches creates enormous synergies leading to a significant advance in the field of organic semiconductors.

In this review we focus on oligomeric/molecular films, as we believe that the control of molecular structures and interfaces provides highly defined systems which allows, on the one hand, the study of the basic physics and, on the other hand, to find the important parameters necessary to improve organic devices.

Even the simplest organic devices have a number of constituents whose morphology, order, and interfaces have a major influence on their properties. This book is conceived to report on the activities of the leading groups in Austria and their international collaborators, who work in the field of growth and characterisation of organic films and devices and focus on the fabrication and characterisation of highly ordered functional organic films. The wide range of expertise of the contributing groups allows the combination of different methodologies and aspects of physics,

chemistry, and materials science for the design and understanding of well-defined organic structures.

Our vision is that functional organic molecules can be the basic building blocks for both low cost large area and new nano-scale devices, ranging from solar cells to chemical sensors. Because of the technological relevance and the applications that can be imagined for devices incorporating organic films it is important to understand the fundamental processes of organic film formation, the structures that are formed, their interfaces and their properties.

The scope of this book is such that it bridges the gap between fundamental research and basic applied sciences. This will contribute to new concepts and a knowledge base, which will have a direct impact in the fields of electronic, opto-electronic, and photovoltaic devices, as well as sensors and nanoscopic devices.

Berlin, Germany — Claudia Draxl
Graz, Austria — Michael Ramsey
Linz, Austria — Helmut Sitter

Contents

Contributors

Claudia Draxl Chair of Atomistic Modelling and Design of Materials, Montanuniversität Leoben, Leoben, Austria; Physics Department, Humboldt Universität zu Berlin, Berlin, Germany

Siegfried Bauer Department of Soft Matter Physics, Johannes Kepler University Linz, Linz, Austria

Giovanni Bongiovanni Dipartimento di Fisica, Università di Cagliari, Monserrato, (CA), Italy

Tatjana Djuric Institute of Solid State Physics, Graz University of Technology, Graz, Austria

Matthias Edler Chair of Chemistry of Polymeric Materials, University of Leoben, Leoben, Austria

Ivan I. Fishchuk Department of Theoretical Physics, Institute for Nuclear Research, National Academy of Sciences of Ukraine, Kyiv, Ukraine

Alexander J. Fleming Surface and Interface Physics, Institute of Physics, Karl-Franzens University Graz, Graz, Austria

Eric D. Głowacki Physical Chemistry, Linz Institute for Organic Solar Cells, Johannes Kepler University Linz, Linz, Austria

Thomas Griesser Chair of Chemistry of Polymeric Materials, University of Leoben, Leoben, Austria

Gerardo Hernandez-Sosa Semiconductor- and Solid State Physics, Johannes Kepler University Linz, Linz, Austria; Innovation Lab GmbH, Heidelberg, Germany

Gregor Hlawacek Physics of Interfaces and Nanomaterials, MESA+ Institute for Nanotechnology, University of Twente, Enschede, The Netherlands

Mihai Irimia-Vladu Physical Chemistry, Linz Institute for Organic Solar Cells, Johannes Kepler University Linz, Linz, Austria; Department of Soft Matter Physics,

Johannes Kepler University Linz, Linz, Austria; Division of Surface Technologies and Photonics, Department of Materials, Joanneum Research Forschungsgesellschaft mbH, Weiz, Austria

Andrey Kadashchuk Department of Photoactivity, Institute of Physics, National Academy of Sciences of Ukraine, Kyiv, Ukraine; Department of Polymer and Molecular Electronics, IMEC, Leuven, Belgium

Wolfgang Kern Chair of Chemistry of Polymeric Materials, University of Leoben, Leoben, Austria

Fawad S. Khokhar Physics of Interfaces and Nanomaterials, MESA+ Institute for Nanotechnology, University of Twente, Enschede, The Netherlands

Georg Koller Surface and Interface Physics, Institute for Physics, Karl-Franzens University Graz, Graz, Austria

Andrea Mura Dipartimento di Fisica, Università di Cagliari, Monserrato, (CA), Italy

Dimitrii Nabok Chair of Atomistic Modelling and Design of Materials, Montanuniversität Leoben, Leoben, Austria; Physics Department, Humboldt Universität zu Berlin, Berlin, Germany

Martin Oehzelt Helmholtz Zentrum Berlin für Materialien und Energie GmbH, BESSY II, Berlin, Germany; Institut für Physik, Humboldt-Universität zu Berlin, Berlin, Germany

Almantas Pivrikas Physical Chemistry, Linz Institute for Organic Solar Cells, Johannes Kepler University Linz, Linz, Austria; Centre for Organic Photonics and Electronics, School of Chemistry and Molecular Biosciences, University of Queensland, Brisbane, Australia

Bene Poelsema Physics of Interfaces and Nanomaterials, MESA+ Institute for Nanotechnology, University of Twente, Enschede, The Netherlands

Peter Puschnig Chair of Atomistic Modelling and Design of Materials, Montanuniversität Leoben, Leoben, Austria; Institute of Physics, Karl-Franzens University Graz, Graz, Austria

Francesco Quochi Dipartimento di Fisica, Università di Cagliari, Monserrato, (CA), Italy

Michael G. Ramsey Surface and Interface Physics, Institute for Physics, Karl-Franzens University Graz, Graz, Austria

Roland Resel Institute of Solid State Physics, Graz University of Technology, Graz, Austria

Lorenz Romaner Chair of Atomistic Modelling and Design of Materials, Montanuniversität Leoben, Leoben, Austria

Michele Saba Dipartimento di Fisica, Università di Cagliari, Monserrato, (CA), Italy

Ingo Salzmann AG Supramolecular Systems, Department of Physics, Humboldt-Universität zu Berlin, Berlin, Germany

N. Serdar Sariciftci Physical Chemistry, Linz Institute for Organic Solar Cells, Johannes Kepler University Linz, Linz, Austria

Günther Schwabegger Semiconductor- and Solid State Physics, Johannes Kepler University Linz, Linz, Austria

Clemens Simbrunner Semiconductor- and Solid State Physics, Johannes Kepler University Linz, Linz, Austria

Helmut Sitter Semiconductor- and Solid State Physics, Johannes Kepler University Linz, Linz, Austria

Philipp Stadler Physical Chemistry, Linz Institute for Organic Solar Cells (LIOS), Johannes Kepler University of Linz, Linz, Austria

Lidong Sun Institute of Experimental Physics, Johannes-Kepler University Linz, Linz, Austria

Christian Teichert Institute of Physics, Montanuniversitaet Leoben, Leoben, Austria

Anna M. Track Surface and Interface Physics, Institute for Physics, Karl-Franzens University Graz, Graz, Austria; NXP Semiconductors Austria GmbH Styria, Gratkorn, Austria

Gregor Trimmel Institute for Chemistry and Technology of Materials, Graz University of Technology, Graz, Austria

Mujeeb Ullah Semiconductor- and Solid State Physics, Johannes Kepler University Linz, Linz, Austria; Centre for Organic Photonics & Electronics (COPE), School of Mathematics and Physics, University of Queensland, Brisbane, QLD, Australia

Raoul van Gastel Physics of Interfaces and Nanomaterials, MESA+ Institute for Nanotechnology, University of Twente, Enschede, The Netherlands

Irene Watzinger Semiconductor- and Solid State Physics, Johannes Kepler University Linz, Linz, Austria

Adolf Winkler Institute of Solid State Physics, Graz University of Technology, Graz, Austria

Harold J.W. Zandvliet Physics of Interfaces and Nanomaterials, MESA+ Institute for Nanotechnology, University of Twente, Enschede, The Netherlands

Peter Zeppenfeld Institute of Experimental Physics, Johannes-Kepler University Linz, Linz, Austria

Part I
Theory

Chapter 1
The Structure of Molecular Orbitals Investigated by Angle-Resolved Photoemission

Peter Puschnig, Georg Koller, Claudia Draxl, and Michael G. Ramsey

Abstract In this contribution, it is shown how the combination of angle-resolved photoemission spectroscopy (ARPES) with ab-initio electronic-structure calculations within the framework of density-functional theory (DFT) leads to insights into electronic and structural properties of organic molecular layers well beyond conventional density-of-sates or $E(k)$ investigations. In particular, we emphasize the rather simple, but for many cases sufficiently accurate, connection between the observed angular dependence of the photocurrent with the spatial distribution of the molecular orbital from which it is arising. After discussing the accuracy and limitations of this approach, which is based on a plane-wave approximation of the final state, three examples are presented. The first utilizes the characteristic angular pattern of the highest occupied molecular orbitals (HOMO) in a pentacene multilayer film in order to measure the molecular tilt angle in the film. In the second example, the nature of two closely spaced molecular emissions from a porphyrin thin film is unambiguously identified as HOMO and HOMO-1, and the molecule's azimuthal alignment is determined. Finally, for a monolayer of para-sexiphenyl on Cu(110), it is demonstrated how the real-space distribution of the filled LUMO and the HOMO of para-sexiphenyl can be reconstructed from the angular dependence of the photocurrent.

P. Puschnig (✉) · C. Draxl
Chair of Atomistic Modelling and Design of Materials, Montanuniversität Leoben,
Franz-Josef-Straße 18, 8700 Leoben, Austria
e-mail: peter.puschnig@uni-graz.at

Present address:
P. Puschnig
Institute of Physics, Karl-Franzens University Graz, Universitätsplatz 5, 8010 Graz, Austria

Present address:
C. Draxl
Physics Department, Humboldt Universität zu Berlin, Zum Großen Windkanal 6, 12489 Berlin, Germany

G. Koller · M.G. Ramsey
Institute of Physics, Karl-Franzens University Graz, Universitätsplatz 5, 8010 Graz, Austria

H. Sitter et al. (eds.), *Small Organic Molecules on Surfaces*,
Springer Series in Materials Science 173, DOI 10.1007/978-3-642-33848-9_1,

1.1 Introduction

Electronic orbitals are the prime determinants of the respective compounds' chemical, electronic, and optical properties. Therefore, the knowledge of energetic positions, ordering, and spatial extent of molecular orbitals is of great interest. However, the valence bands of large conjugated molecules consist of a multitude of closely spaced molecular states, which makes their correct assignment challenging both experimentally and theoretically.

Experimentally, energy positions of molecular orbitals in organic molecular layers can be studied by ultra-violet photoemission spectroscopy (UPS) [1] or by scanning tunneling spectroscopy (STS) [2–7]. UPS has the advantage that accessible binding energies are not limited to a few electron volts from the Fermi level as in STS. However, UPS spectra of thin molecular layers on metals often show only weak and rather broad features and are, therefore, not always conclusive. Also, UPS data depend on the experimental geometry, molecular orientation, and photon energy, which further complicates the assignment of the measured peaks. Moreover, experimental techniques which are probing the *spatial* structure of individual orbitals are rare, and the interpretation of experimental data is commonly difficult and requires guidance from theory [8]. Here, scanning tunneling microscopy (STM) has proven to be a powerful technique for mapping orbital structures of rather complex molecules [2]. However, strong bonding interactions with the substrate make the interpretation of the images in terms of orbital structures problematic [9].

Angle-resolved photoelectron spectroscopy (ARPES), on the other hand, is *the* technique to study the band structure of solids by measuring the kinetic energy of the photoemitted electrons versus their angular distribution [10]. Particularly, many questions in nanophysics and interface engineering are often addressed by this experimental technique which, in combination with density-functional-theory calculations, leads to important physical insight. Recently, however, it has been shown that ARPES provides an alternative route to obtain information regarding the spatial structure of individual molecular orbitals [11–14]. By making certain assumptions about the photoemisson transition matrix element, ARPES intensity maps can also provide useful information regarding orbital structures. Specifically, it has become possible to obtain the one-dimensional wave functions of quantum-well states on nano-structured gold surfaces [13, 15], and the two-dimensional spatial electron distribution in the frontier orbitals of organic π-conjugated molecules adsorbed at metallic surfaces [12, 14].

In this contribution, we review the recent progress in measuring the spatial structure of molecular orbitals by using angle-resolved photoemission spectroscopy. By comparing measured ARPES data with simulations of the photoemission intensity based on density-functional theory, we demonstrate the strength of this method which lies in the direct and easy-to-apply connection between the measured angular dependence of the photocurrent and the Fourier transform of the molecular orbital from which electrons are emitted. First, we will give a brief account on the theoretical description which is based on the one-step model of photoemission. The implication of using a plane wave for the final state will be shown, and the limits of this approximation will be discussed. Then, three examples for molecular

films consisting of highly oriented multi-layers of π-conjugated molecules down to monolayers adsorbed at metallic surfaces will be given: First, results for a pentacene multilayer film are shown for which the tilt angle of the molecules could be determined from a comparison between the ARPES data and momentum maps of the free molecule. Second, data for a monolayer of tetraphenyl porphyrine on Cu(110) demonstrate the strength of the method in identifying of molecular orbitals and determining azimuthal molecular orientations. Finally, for a monolayer of para-sexiphenyl on Cu(110) it is demonstrated how ARPES momentum maps of the former lowest unoccupied molecular orbital (LUMO) and the highest occupied molecular orbital (HOMO) are utilized to reconstruct real-space distributions of the respective orbitals.

1.2 Theory

Photoemission spectroscopy is commonly applied to study the band structure of solids by measuring the kinetic energy versus angular distribution of the photoemitted electrons. Here we show that this experimental technique can also be used to gain information on the spatial electron distribution in molecular orbitals [12]. In angle-resolved photoemission spectroscopy (ARPES), schematically depicted in Fig. 1.1, an incident photon of energy $\hbar\omega$ excites an electron from a bound initial state, described by wave function ψ_i and energy E_i, to a final electron state ψ_f with kinetic energy E_{kin}. Because energy and momentum parallel to the surface are conserved during the photoemission process, the measurement of the emitted electron's energy and momentum probes the band structure of solids. Thus, ARPES is commonly used to study band dispersions, Fermi surfaces and many-body correlations in a wide range of materials [16].

1.2.1 One-Step Model of Photoemission

A theoretical description of the angle-resolved photoelectron intensity is generally rather involved, and attempts to compute it in a quantitative manner are rather scarce. Within this work, photo-excitation is treated as a single coherent process from a molecular orbital to the final state which is referred to as the one-step model of photoemission (PE). The PE intensity $I(\theta, \phi; E_{\mathrm{kin}})$ is given by a Fermi golden rule formula [17]

$$I(\theta, \phi; E_{\mathrm{kin}}) \propto \sum_i \left| \left\langle \psi_f(\theta, \phi; E_{\mathrm{kin}}) | \mathbf{A} \cdot \mathbf{p} | \psi_i \right\rangle \right|^2 \times \delta(E_i + \Phi + E_{\mathrm{kin}} - \hbar\omega). \quad (1.1)$$

Here, the polar and azimuthal emission angles defined in Fig. 1.1 are denoted by θ and ϕ, respectively. The photocurrent I is given by a sum over all transitions from occupied initial states i described by wave functions ψ_i to the final state ψ_f

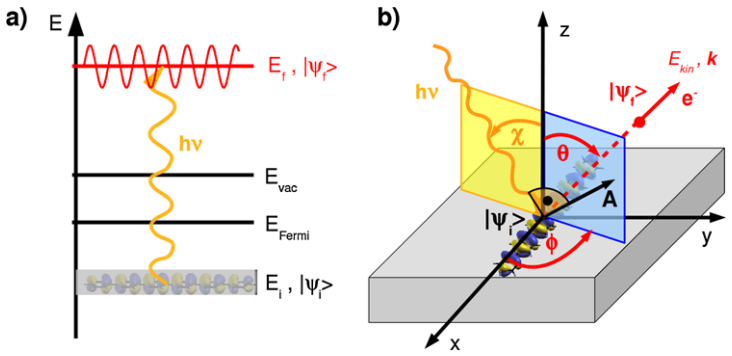

Fig. 1.1 (**a**) Schematic energy level diagram of a photoemission experiment showing the energy of the initial state, E_i, the Fermi level E_F, the vacuum level E_{vac}, and the final-state energy E_f. (**b**) In angle-resolved photoemission spectroscopy, an incident photon with energy $h\nu$ and vector potential $\mathbf{A}$ excites an electron from the initial state ψ_i to the final state ψ_f characterized by the kinetic energy E_{kin} and the momentum vector $\mathbf{k}$. The polar and azimuthal angles θ and ϕ, respectively, define the direction of the photoemitted electron

characterized by the direction (θ, ϕ) and the kinetic energy of the emitted electron. The delta function ensures energy conservation, where Φ denotes the sample work function. The transition matrix element is given in the dipole approximation, where $\mathbf{p}$ and $\mathbf{A}$, respectively, denote the momentum operator and the vector potential of the exciting electro-magnetic wave.

Plane-Wave Approximation

The difficult part in evaluating Eq. (1.1) is the proper treatment of the final state. In the most simple approach, it is approximated by a plane wave (PW) only characterized by the direction and wave number of the emitted electron. This has already been proposed more than 30 years ago [18] with some success in explaining the observed PE distribution from atoms and small molecules adsorbed at surfaces. Using a plane-wave approximation is appealing since the evaluation of Eq. (1.1) renders the photocurrent I_i arising from one particular initial state i proportional to the Fourier transform $\tilde{\psi}_i(\mathbf{k})$ of the initial-state wave function corrected by the polarization factor $\mathbf{A} \cdot \mathbf{k}$:

$$\left|\tilde{\psi}_i(\mathbf{k})\right| \propto \frac{\sqrt{I_i(\theta, \phi)}}{|\mathbf{A} \cdot \mathbf{k}|}. \tag{1.2}$$

Thus, if the angle-dependent photocurrent of individual initial states can be selectively measured (as it can for organic molecules where the intermolecular band dispersion is often smaller than the energetic separation of individual orbitals), a one-to-one relation between the photocurrent and the molecular orbitals in reciprocal space can be established. This allows the measurement of the absolute value

of the initial-state wave function in reciprocal space and, via a subsequent Fourier transform, a reconstruction of molecular orbital densities in real space.

Limitations of the Plane-Wave Approximation

It has been observed rather early that the plane-wave final-state approximation had problems in describing the photoemission intensity of some large polyatomic molecules and/or certain experimental geometries [19, 20]. This led to the conclusion that the plane-wave final-state approximation should not be used and nourished the development of the so-called independent-atomic-center (IAC) approximation [21]. In the IAC approximation, the initial state is decomposed into atomic eigenfunctions which build up the initial molecular orbitals, while the final state is composed of scattering solutions of the atomic Schrödinger equation at the final-state energy $E_k = \frac{\hbar^2}{2m}k^2$. The transition matrix element is then given by a coherent sum over these initial and final states, respectively. Thus, the IAC expression for the photoelectron wave function A with kinetic energy E_{kin} at the detector position $\mathbf{R}$ can be written in the following form [21]:

$$A(\mathbf{R}, E_{\mathrm{kin}}) = \sum_{\alpha} \sum_{nlm} C_{\alpha,nlm} e^{i\mathbf{k}\mathbf{R}_\alpha} \sum_{LM} M^{LM}_{\alpha,nlm}(E_{\mathrm{kin}}) Y_{LM}(\hat{R}). \tag{1.3}$$

Here, the initial orbital $\psi_i(\mathbf{r})$ is expressed as a linear combination of atomic orbitals $\phi_{\alpha,nlm}$ centered at the position $\mathbf{R}_\alpha$, where nlm represent the principal and angular-momentum quantum numbers of the orbital and α the atomic center on which it resides:

$$\psi(\mathbf{r}) = \sum_{\alpha} \sum_{nlm} C_{\alpha,nlm} \phi_{\alpha,nlm}(\mathbf{r} - \mathbf{R}_\alpha). \tag{1.4}$$

The matrix elements $M^{LM}_{\alpha,nlm}$ in Eq. (1.3) are dipole matrix elements between the atomic wave functions $\phi_{\alpha,nlm}$ and solutions of the Schrödinger equation in an atomic potential at the energy E_{kin} and angular momentum LM.

The goal of the remaining part of this section is to shed light on the relation between the IAC and the simpler PW approach and to hint towards possible limitations of the latter. It was already noted by Grobman that expression (1.3) can be considerably simplified if the initial molecular orbital is comprised of atomic orbitals of the same chemical and orbital character. A specific example of such a situation is given by a π molecular orbital of a planar polyatomic molecule. Then the coefficients $C_{\alpha,nlm}$ are only non-zero for atomic p_z orbitals and only one term remains of the sum over nlm:

$$A(\mathbf{R}, E_{\mathrm{kin}}) = \sum_{\alpha} C_{\alpha,2p_z} e^{i\mathbf{k}\mathbf{R}_\alpha} \sum_{LM} M^{LM}_{2p_z}(E_{\mathrm{kin}}) Y_{LM}(\hat{R}). \tag{1.5}$$

In the above expression we have also omitted the atomic index α in the transition matrix elements since they do not depend on the position of the atom but only on the

type of atomic orbital which is assumed to be $2p_z$ for all contributing atoms. Thus, the sum over the final-state angular-momentum quantum numbers LM, the atomic factor, which we abbreviate as

$$N_{2p_z}(E_{\mathrm{kin}}, \hat{R}) = \sum_{LM} M_{2p_z}^{LM}(E_{\mathrm{kin}}) Y_{LM}(\hat{R}), \tag{1.6}$$

can be put in front of the summation over atoms α and we are left with the simplified expression for the photoemission amplitude at the detector:

$$A(\mathbf{R}, E_{\mathrm{kin}}) = N_{2p_z}(E_{\mathrm{kin}}, \hat{R}) \sum_{\alpha} C_{\alpha,2p_z} e^{i\mathbf{k}\mathbf{R}_\alpha}. \tag{1.7}$$

As has been noted by Grobman [21] the term $N_{2p_z}(E_{\mathrm{kin}}, \hat{R})$ acts only as a weakly varying envelope function while the main angular dependence of the photoemission intensity is dominated by the last term in Eq. (1.7), which is closely related to the Fourier transform of the initial molecular orbital. By taking the Fourier transform (FT) on both sides of Eq. (1.4) we see that the FT of the initial molecular orbital $\tilde{\psi}(\mathbf{k})$ can be written as

$$\tilde{\psi}(\mathbf{k}) = \tilde{\phi}_{2p_z}(\mathbf{k}) \sum_{\alpha} C_{\alpha,2p_z} e^{i\mathbf{k}\mathbf{R}_\alpha}. \tag{1.8}$$

Here, we have introduced the FT of a p_z orbital, $\tilde{\phi}_{2p_z}(\mathbf{k})$, whose angular part is simply given by the spherical harmonic, $Y_{10}(\theta, \phi) \propto \cos\theta$ [18].

Equivalence of IAC and PW Approximation

For large π conjugated molecules, the main angular dependence will be determined by the last term in Eq. (1.7). By combining Eqs. (1.7) and (1.8) we see that the IAC produces a result which is in fact very similar to the PW final-state assumption, compare Eq. (1.2), provided that the initial molecular orbital is composed of atomic orbitals of the same type as is the case for planar π conjugated molecules:

$$A(\mathbf{R}, E_{\mathrm{kin}}) = \left(\frac{N_{2p_z}(E_{\mathrm{kin}}, \hat{R})}{\tilde{\phi}_{2p_z}(\mathbf{k})} \right) \times \tilde{\psi}(\mathbf{k}). \tag{1.9}$$

Last but not least we note that the prefactor, $N_{2p_z}/\tilde{\psi}_{2p_z}$ can be shown to become completely independent of the emission direction (θ, ϕ) for the special case where the polarization vector $\mathbf{A}$ of the photon is exactly parallel to the emission direction $\mathbf{k}$. For this particular geometry the photoemission intensity resulting from the IAC, which is the square of $A(\mathbf{R}, E_{\mathrm{kin}})$, reduces exactly to the intensity emerging from the plane-wave final-state assumption. This observation has already been made by Goldberg for the photoemission cross section from atoms [22]. Moreover, due to the overall weak angular dependence of the envelope factor $N_{2p_z}/\tilde{\psi}_{2p_z}$, the Fourier

transform of the initial molecular orbital $\tilde{\psi}(\mathbf{k})$ continues to provide a good description of the angle-dependent PE intensity also when the direction of the polarization vector deviates from the emission direction. Hence it is expected that the difference between the PW result, Eq. (1.2), and the IAC expression, Eq. (1.8), only grows weakly with the deviation from the above mentioned condition.

Summary of Theoretical Consideration

From what was said above, the plane-wave final-state assumption can be expected to be valid if the following conditions are fulfilled: (i) π orbital emissions from large planar molecules, (ii) an experimental geometry in which the angle between the polarization vector $\mathbf{A}$ and the direction of the emitted electron $\mathbf{k}$ is rather small, and (iii) molecules consisting of many light atoms (H, C, N, O). The latter requirement is a result of the small scattering cross section of light atoms and the presence of many scattering centers expected to lead to a rather weak and structureless angular pattern [11, 23]. With these conditions satisfied, a one-to-one mapping between the PE intensity and individual molecular orbitals in reciprocal space is possible, providing a valuable tool for the investigation of organic molecular films and monolayers. This will be demonstrated with several examples in the following sections.

1.3 Photoemission Experiments

Presently, there are a number of display-type analyzers that are capable of obtaining angular-dependent photoemission intensity maps suitable for our approach [24]. Our ARPES experiments are performed at room temperature using a toroidal electron-energy analyzer described elsewhere [25] attached to the TGM-4 beamline at the synchrotron radiation facility BESSY II. This toroidal electron analyzer allows simultaneous collection of photoelectrons in a kinetic energy window of 0.8 eV over a polar angle θ range of 180° in the specular plane. Azimuthal scans are then made by rotating the sample around the surface normal in 1° steps for >180° of azimuthal angle ϕ. The angular emission data are then converted to momentum $k_{\parallel}$ using the formula $k_{\parallel} = \sqrt{2m_e E_{\mathrm{kin}}/\hbar^2}\sin\theta$ [$\mathrm{\AA}^{-1}$] to create the momentum maps. The photon incidence angle is $\alpha = 40°$, and the polarization direction is always in the specular plane. A photon energy of $h\nu = 35$ eV is used throughout.

1.4 Results

In this section, we demonstrate the viability of the simple plane-wave final-state approach in conjunction with initial-state orbitals taken from density-functional theory for a number π-conjugated organic molecules. First, we present data for the

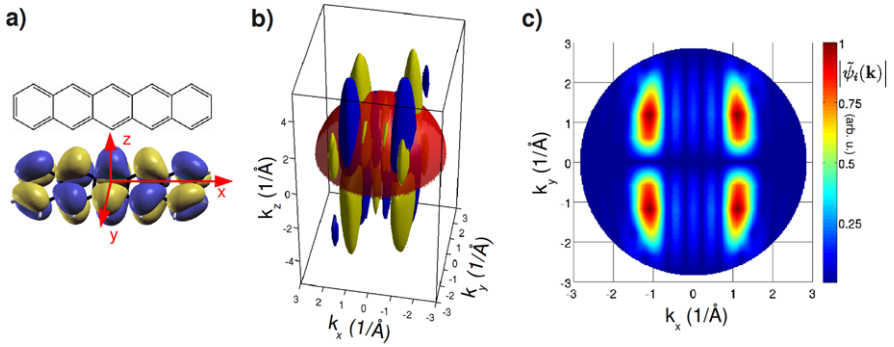

Fig. 1.2 (**a**) Chemical structure of pentacene and its highest molecular orbital (HOMO) calculated from density-functional theory. (**b**) Three-dimensional Fourier transform of the pentacene HOMO orbital, *yellow* (*blue*) showing an isosurface of a constant positive (negative) value. The *red hemisphere* illustrates a region of constant kinetic energy as explained in the text. (**c**) Absolute value of the pentacene HOMO Fourier transform on the hemisphere indicated in panel (**b**)

well-known molecular semiconductor pentacene in a multilayer thin film. Here, we focus on the emission from the HOMO and show that ARPES momentum maps—when compared to calculations—allow for a precise determination of the molecular tilt angle. As a second example, we compare ARPES momentum maps of a monolayer of tetraphenyl porphyrine with calculations of the PE intensity allowing for an identification of the HOMO and HOMO-1 and the determination of the azimuthal molecular orientation. Thirdly, we demonstrate that in certain cases the PW final-state approach enables a reconstruction of real-space orbitals. Here, we show ARPES data of a monolayer of para-sexiphenyl bonded to the Cu(110) surface. Not only are we able to reconstruct a real-space image of the HOMO but we also show that the PE intensity at the Fermi level that appears on adsorption has the orbital structure of the lowest unoccupied molecular orbital (LUMO).

1.4.1 Determination of Molecular Orientations

Pentacene is a planar aromatic molecule consisting of five linearly edge-fused phenyl rings, and has been extensively studied due to its interesting opto-electronic properties. Its electronic structure, in particular the intermolecular HOMO dispersion, has been analyzed by means of both photoemission experiments [26–28] and calculations within the framework of density-functional theory [29–31].

To illustrate the relation between the measured PE intensity and the FT of the emitting orbital, we calculate the electronic structure of an isolated pentacene molecule using DFT [32]. The resulting HOMO orbital is depicted in Fig. 1.2a, and its corresponding three-dimensional FT in Fig. 1.2b. Because the momentum maps are measured at constant binding energy, we evaluate the FT on a hemisphere of radius $k = \sqrt{(2m/\hbar^2)E_{\mathrm{kin}}}$ (indicated in red). The value of the FT on that hemisphere

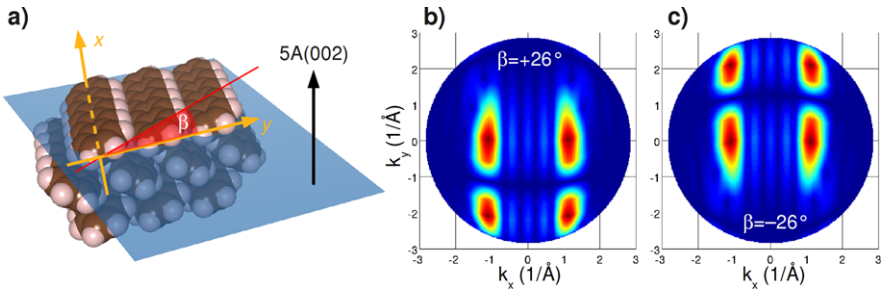

Fig. 1.3 (**a**) Geometry of the (002) plane of pentacene crystal structure exhibiting flat lying molecules with a tilt angle of $\beta = 26°$. (**b**) Simulated Fourier transform of the pentacene HOMO of a molecule with a tilt angle of $\beta = 26°$. (**c**) Same as (**b**) but for a tilt angle of $\beta = -26°$

for a kinetic energy of 29.8 eV is shown in Fig. 1.2c. We observe four main intensity maxima centered around ($k_x = 1.15,\ k_y = 1.2$) Å^{-1} and symmetrically located around the Γ point (normal emission). For emission planes parallel (perpendicular) to the long (short) molecular axis, i.e., in the xz and yz planes, respectively, a vanishing photoemission intensity is predicted. This fact is reflecting the nodal structure of the pentacene HOMO orbital.

When the molecule is vacuum deposited on the p(2x1) oxygen reconstructed Cu(110) surface, its long axis orients parallel to the oxygen rows, resulting in crystalline pentacene(022) films [33] as depicted in Fig. 1.3a. When comparing the theoretical results of Fig. 1.2 with the experimental ARPES data of a multilayer of pentacene grown on a Cu(110)-(2x1)O substrate, one has to consider the orientation of the molecules in this multilayer film. From X-ray diffraction pole-figure measurements [33], the contact plane is determined to be the (022) crystallite orientation. As visualized in Fig. 1.3, this surface termination exhibits molecules with their long axis parallel to the surface but the π face tilted out of the surface plane by an angle of $\beta = 26°$. When this tilt angle is taken into account in the calculation of the Fourier transform, the four main lobes described above are shifted in y direction. This is illustrated in Figs. 1.3b and c, which show the pentacene HOMO of a molecule with a tilt angle of $\beta = 26°$ and $\beta = -26°$, respectively.

In the multilayer film, an effective average of the two molecular orientations, $+26°$ and $-26°$, is to be expected due to the two-fold symmetry of the substrate surface. In Fig. 1.4, we therefore compute an average of the results for $\beta = 26°$ and $\beta = -26°$. Figure 1.4 also shows an experimental momentum map, at the HOMO energy of a pentacene multilayer using a toroidal electron-energy analyzer at the synchrotron radiation facility BESSY II [25]. As a function of the momentum vector parallel to the molecular axis, k_x, there is a pronounced intensity maximum of the photoemission intensity centered at 1.15 Å^{-1}, as observed previously [28]. In the momentum maps, we see that these intense features extend about ± 0.8 Å^{-1} in k_y direction, and, in addition, there are weaker intensity lobes at about the same k_x value around $k_y \approx \pm 2$ Å^{-1}. The comparison between the simulated momentum map (Fig. 1.4a) and the measurement (Fig. 1.4b) is very satisfying. In particular, the

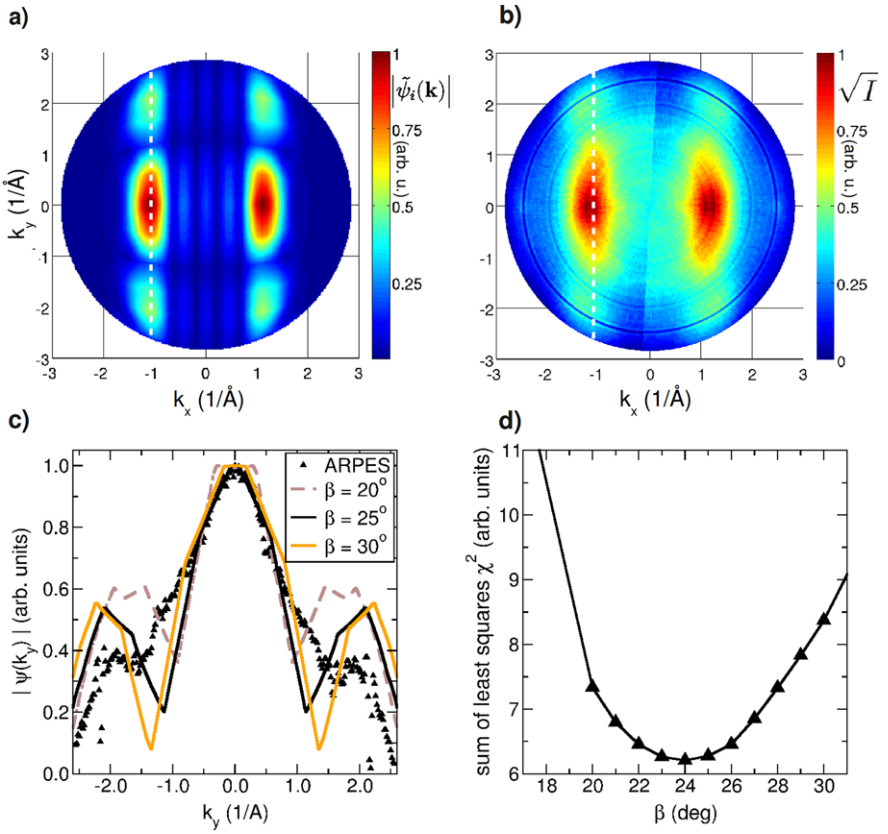

Fig. 1.4 (**a**) The sum of the data shown in Figs. 1.3b and c corresponding to the experimental situation where both tilts will be present. (**b**) Experimental photoemission intensity at a constant binding energy corresponding to the pentacene HOMO from the multilayer of pentacene as described in the text. (**c**) Experimental (*symbols*) vs. theoretical (*lines*) line scans at $k_x = -1.1$ Å as indicated by the *white dashed line* in (**a**) and (**b**). Simulations for three different tilt angles β are shown, 20° (*brown*, *dashed*), 25° (*black*, *solid*), 30° (*orange*). (**d**) Difference between experiment and simulation expressed as the sum of squared differences versus pentacene tilt angle β

maxima at the $k_y = 0$ line are clearly found to originate from the tilt angle of the molecules. Both the strong maxima at $k_y = 0$ and the weak peaks at $k_y = 2$ Å^{-1} result from the out-of-plane tilt angle of the pentacene molecules. Clearly, the FT approach describes the PE intensity well and therefore allows molecular orientations to be determined.

In order to emphasize the sensitivity of the PE intensity on the tilt angle we show a line scan along k_y at constant $k_x = -1.1$ Å as indicated by the white dashed line in Fig. 1.4a. These plots are shown in Fig. 1.4c where we compare the experimental line scan (symbols) with our simulated PE intensity for three different tilt angles β of the pentacene molecule. Clearly, the simulation result for $\beta = 25°$ is in better agree-

ment with the measurement than the computations for 20° and 30°, respectively. In particular, the peak position of the maxima around $k_y \approx \pm 2$ Å^{-1} are shifted to lower (higher) values by decreasing (increasing) the tilt angle. But also the shape of the main feature centered around $k_y = 0$ is reproduced better by the simulation for $\beta = 25°$. To quantify the quality of the simulations for various tilt angles β we also show the sum of the squared differences between the experimental line scans and the simulated ones in Fig. 1.4d. The curve shows a minimum at $\beta = 24°$ which is very close to the value of 26° obtained from X-ray pole-figure measurements on these pentacene multilayer films [33] and assuming the bulk structure from Mattheus and co-workers [34]. Thus, we estimate the accuracy of the ARPES approach to determine molecular tilt angles better than 5°. Compared to alternative methods, such as NEXAFS, the ARPES approach has the added advantage that rather than giving an average orientation, multiple orientations are immediately apparent and can be resolved. Moreover, ARPES works at low photon energies, minimizing damage to the sample, and does not require a tunable photon source.

1.4.2 Identification of Molecular Orbitals

In this section, it is demonstrated how ARPES momentum maps can be utilized to identify molecular states of organic molecules adsorbed on metallic surfaces beyond a simple comparison of calculated orbital energies with energy-distribution curves measured by UPS. As an example, we choose porphyrines which are of interest as versatile materials for organic electronics due to their tendency to form π–π stacked layers. In particular, thin films of tetraphenyl porphyrin, $C_{44}H_{30}N_4$, (H_2TPP) deposited on the oxygen reconstructed Cu(110)-(2x1)O surface have been shown to produce well-ordered, epitaxially aligned porphyrin thin films [35].

As can be seen from Fig. 1.5a, H_2TPP molecules consists of a highly conjugated porphyrin skeleton (macrocycle) in which two hydrogen atoms are attached to two out of four nitrogen atoms sitting in the center of the molecule. The macrocycle is surrounded by four phenyl rings which are tilted out of the porphyrin plane. Figure 1.5 shows the optimized geometry of an isolated H_2TPP molecule as obtained from DFT by using a generalized gradient approximation [36] for exchange-correlation effects together with a density-of-states plot (b) and orbital pictures of the HOMO (c) and HOMO-1 (d). At the GGA-DFT level, the two highest occupied orbitals, the HOMO and HOMO-1, are separated by 0.4 eV followed by two closely spaced states at about 1 eV binding energy. The LUMO is separated from the HOMO by a GGA-DFT gap of about 1.7 eV. Focusing on the HOMO and HOMO-1, we observe distinct nodal patterns which should also be reflected in the respective momentum maps thereby allowing for a clear distinction of these two orbitals. For instance, the HOMO is both symmetric about the xz plane and about the yz plane, while the HOMO-1 is anti-symmetric about these two planes, i.e., exhibits nodal planes in the xz and yz planes.

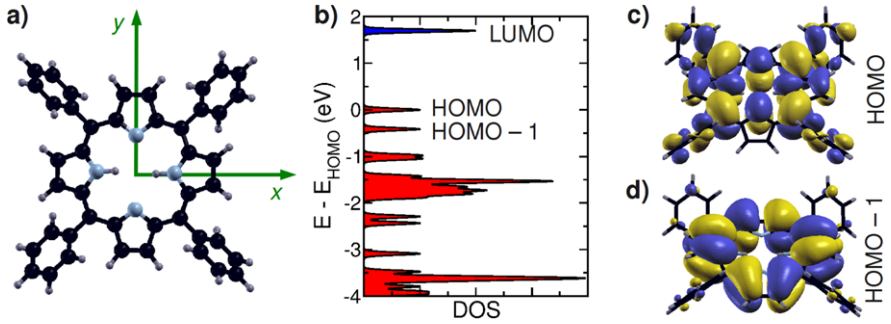

Fig. 1.5 (**a**) Chemical structure of tetraphenyl porphyrine with two hydrogen atoms saturating the bonds at the center of the molecule (H_2TPP). (**b**) Density of states of an isolated H_2TPP molecule as obtained from density-functional theory and a generalized gradient approximation for the exchange-correlation potential. (**c**) and (**d**) are corresponding orbital pictures of the HOMO and HOMO-1 separated by 0.4 eV

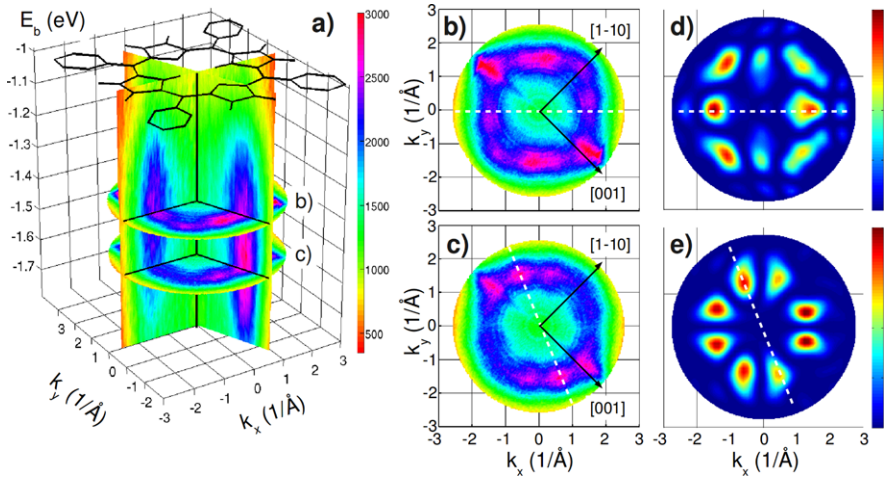

Fig. 1.6 (**a**) Experimental photoemission intensity (*color coded*) of a H_2TPP film as a function of binding energy E_b and momenta k_x and k_y, respectively. Two 'horizontal' sections at constant binding energies, -1.38 and -1.55 eV, as well as two 'vertical' sections at $k_y = 0$ and at an angle of $-22°$ from k_x are shown. Panels (**b**) and (**c**) display those constant binding energy momentum maps corresponding to $E_b = -1.38$ and -1.55 eV, respectively. Panels (**d**) and (**e**) are simulated momentum maps corresponding the H_2TPP HOMO and HOMO-1, respectively

In Fig. 1.6, ARPES data of a thin film of H_2TPP on Cu(110)-(2x1)O with a nominal thickness of 6 Å are compared to simulated momentum maps of the isolated molecule. By using 35 eV photons and the toroidal electron-energy analyzer at BESSY II, an energy window from about -1.0 to -1.8 eV below the Fermi level has been scanned. Further, by collecting electrons with a polar angle span from -70 to $+70°$ and by azimuthally rotating the sample around 180°, a comprehensive data

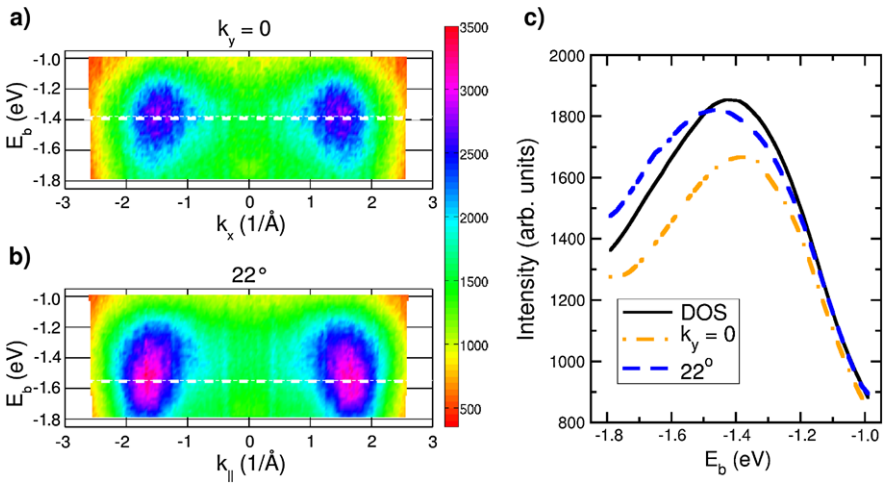

Fig. 1.7 (**a**) Band map of a H_2TPP film in the xz emission plane. (**b**) Same as (**a**) but for an emission plane rotated by $-22°$ with respect to the yz plane as indicated by the 'vertical' sections through the three-dimensional data cube shown in Fig. 1.6. (**c**) Energy-distribution curves (EDC) integrated over the whole k_x–k_y plane (*black line*) as well as for the emission planes shown in (**b**) and (**c**), respectively

set of the photoemission intensity, I, as a function of binding energy E_b and parallel momenta components k_x and k_y has been measured. These ARPES data are visualized in Fig. 1.6a in which the intensity is color-coded and several sections through the data are shown. On the one hand, two 'vertical' sections show the energy and polar angle distribution of the photocurrent for fixed azimuths of the emission plane. These tomographic sections are displayed separately in Fig. 1.7 and are discussed in more detail below. On the other hand, Fig. 1.6a also features two 'horizontal' sections at constant binding energies (CBE), namely at $E_b = -1.38$ and -1.55 eV. For clarity, these CBE momentum maps are also displayed in panels (b) and (c) of Fig. 1.6, respectively. Although quite close in energy, i.e., only 170 meV, the azimuthal intensity distribution appears different. While the map at -1.55 eV exhibits minima along the $k_x = 0$ and $k_y = 0$ directions, the intensity along these directions has clearly increased for the momentum map at -1.38 eV. This is indicative of the distinct symmetries and nodal patterns of the HOMO-1 and HOMO of H_2TPP mentioned earlier.

Indeed, the calculated momentum maps of the isolated molecule's HOMO and HOMO-1 displayed in panels (d) and (e) of Fig. 1.6 also reflect the orbitals' symmetry and their nodal patterns. In addition, also the (k_x, k_y) positions of the intensity maxima can be compared to the measured maps.[1] This comparison lets us conclude that the HOMO of the adsorbed H_2TPP is centered at an energy of -1.38 eV

[1]Note that the intensity maxima close to the substrate's [001] direction are due to a measurement artifact, i.e., a reflection of the primary photon beam into the detector.

whereas its HOMO-1 has a peak at a binding energy of −1.55 eV. It is also evident from the 'vertical' sections in Fig. 1.6a that the HOMO and HOMO-1 resonances are observed over several tenth of an eV and are, therefore, overlapping in energy. Hence, both momentum maps at −1.38 and −1.55 eV show contributions from both HOMO and HOMO-1 and the symmetry and nodal patterns cannot be seen as clearly as in the computed, pure maps. But how could we separate these two orbital resonances and assign to them the above mentioned binding energies?

The key are those 'vertical' sections through $I(E_b, k_x, k_y)$ which can be chosen in such a way as to highlight characteristic features of the respective molecular orbitals. For instance, the HOMO is expected to have maxima along k_x as indicated by the white dashed line in panel (b), while the HOMO-1 has a nodal plane in this direction. Therefore, ARPES scans along this azimuth project out contributions of the HOMO. Similarly, the HOMO-1 has intensity maxima for an emission plane rotated by 22° with respect to the k_y axis (dashed line in panel (c)), while the HOMO has almost vanishing intensity along this azimuth. Hence, this azimuth serves as a fingerprint for the HOMO-1. As can be seen from Fig. 1.6a, this allowed us to assign the energies of −1.38 eV and −1.55 eV to the center of the HOMO and HOMO-1 emissions and determine their energy width to be about 0.5 eV. For clarity, the ARPES band maps at the above mentioned azimuthal directions are also reproduced in Fig. 1.7. Panel (c) of this figure also shows the corresponding energy-distribution curves (EDC) integrated over all polar angles, i.e. parallel momentum values, along the k_x axis (red line) and the 22° azimuth with respect to the k_y axis (blue line). Also, these EDCs exhibit different energy peak positions allowing the HOMO and HOMO-1 to be separated. In contrast, an EDC integrated over the full polar and azimuthal angle dependence, i.e., integrated over the k_x–k_y plane (black line), yields a broad and featureless peak with no possibility to discern the contributions from the two involved orbitals. In summary, the characteristic (k_x, k_y)-dependences of molecular emissions allows their energy position and width to be determined beyond the limit of energy resolution. Our data also show that emission planes not carefully chosen may emphasize or suppress particular molecular orbitals due to selection rules inevitably involved in any photoemission process.

We conclude this section by discussing the azimuthal alignment of the H_2TPP molecules with respect to the Cu(110)-(2x1)O substrate. Tacitly, we have been assuming throughout this section that the molecule's (x, y) coordinate frame is rotated by 45° with respect to the principal substrate directions as already indicated in Fig. 1.6 and visualized more clearly in Fig. 1.8. Indeed, there is evidence for such an alignment from X-ray diffraction pole-figure measurements of 370 Å thick film of H_2TPP/Cu(110)-(2x1)O [35]. For these thicker films, the X-ray diffraction showed the $(5\overline{1}03)$ net plane of the triclinic H_2TPP polymorph crystal structure to be parallel to the substrate surface. In this plane, the porphyrin macrocycle is almost parallel to the substrate surface. Moreover, the epitaxial relationships revealed that the molecules are oriented such that the central hydrogens attached to the nitrogen atoms are pointing towards a 45° direction with respect to the [001] substrate axis [35] as also indicated in Fig. 1.8. In addition to this evidence derived from a 370 Å thick film, also the ARPES data for the 6 Å film reveal the identical alignment. As can be seen from Fig. 1.6, the chosen azimuthal orientation maximizes the

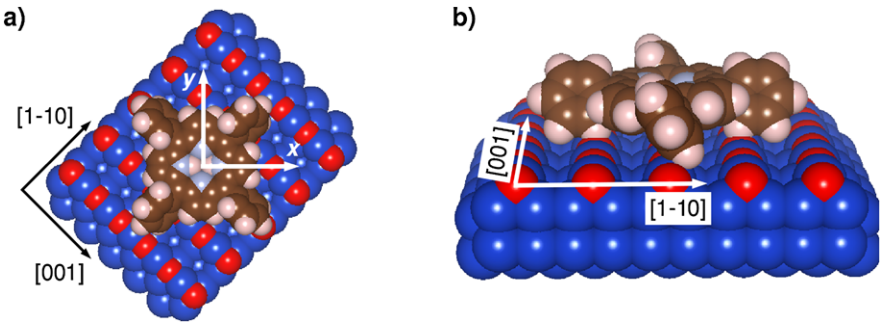

Fig. 1.8 Top (**a**) and side view (**b**) showing the azimuthal alignment of H_2TPP adsorbed on the Cu(110)-(2x1)O substrate. The substrate's [001], i.e., the oxygen row direction, and [1-10] directions are indicated as well as the (x, y) coordinate frame of the molecule which is rotated by 45° about the substrate's principal axes. Copper atoms are colored *dark blue*, oxygens *red*, carbons *dark brown*, nitrogens *light blue*, and hydrogens *light brown*

agreement with the calculated momentum maps for both the HOMO and HOMO-1. Thus, ARPES maps do not only allow molecular emissions to be identified but also enable azimuthal alignments of extremely thin films, down to monolayers, to be determined.

1.4.3 Reconstruction of Molecular Orbitals in Real Space

We continue by demonstrating the viability of the plane-wave approach for both reciprocal space mapping as well as real-space reconstructions of relatively complicated molecular orbitals. Here, we show that this approach allows reconstruction of the orbitals of para-sexiphenyl bonded to the Cu(110) surface. Not only are we able to reconstruct a real-space image of the HOMO but we also show that the PE intensity at the Fermi level that appears on adsorption has the orbital structure of the lowest unoccupied molecular orbital (LUMO).

When deposited on a Cu(110) substrate, sexiphenyl (6P) molecules align with their long molecular axes parallel to the [1-10] azimuth of Cu(110) [37], i.e., parallel to the copper rows and, upon saturation, form a well-ordered monolayer. A structural motif of this adlayer together with the underlying Cu(110) substrate is displayed in Fig. 1.9a. Here, we show the primitive surface unit cell of the saturated adlayer indicated by the blue arrows. This structure has been deduced from both low energy electron diffraction [38] and the STM in Fig. 1.9b. This typical room temperature STM image of a saturated monolayer of sexiphenyl on Cu(110) was obtained with a bias voltage 0.19 V.

In Fig. 1.9c, we show the angle-dependent photoemission of the sexiphenyl monolayer adsorbed on Cu(110) with the emission plane parallel to the long molecular axis. Comparison with equivalent photoemission data for the clean Cu(110) surface identifies the two features indicated by the red arrows as stemming from

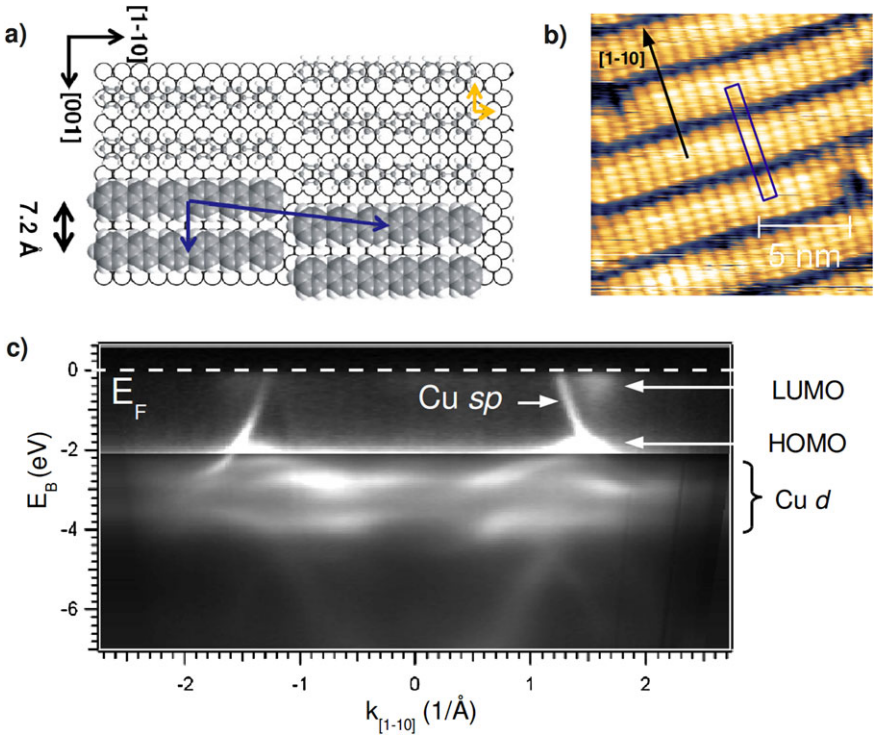

Fig. 1.9 (**a**) Schematic representation of the para-sexiphenyl (6P) monolayer on the Cu(110) surface. The long molecular axis is oriented parallel to the [1-10] direction of the Cu(110) surface, the primitive surface unit cell of the adlayer is indicated by *blue arrows*. (**b**) STM image of the 6P monolayer on the Cu(110) surface. The substrate [1-10] direction is indicated by the *arrow*, and the equivalent centered surface unit cell [c(2x22)] of the 6P adlayer is marked as the *blue rectangle*. (**c**) Angle-resolved photoemission intensity from the 6P monolayer on Cu(110) with an emission plane parallel to the long molecular axis. The *dashed line* indicates the Fermi level and *arrows* point at features that we identify as originating from the sexiphenyl HOMO and LUMO. Between 0 and −2 eV, the *intensity scale* has been magnified for clarity

molecule. The state slightly below the Fermi level is tentatively attributed to the partially filled LUMO, while the newly appearing emission with a binding energy of 1.9 eV is likely due to the sexiphenyl HOMO. The fact that the peaks are at positions in k_x direction which reflect the main spatial periodicity of the sexiphenyl HOMO [39] and LUMO, respectively, is already the first indication for this assignment.

A proof of this assignment can be given by measuring k_x–k_y momentum maps at the constant binding energies corresponding to these features appearing upon adsorption, i.e., at 0.3 and 1.9 eV below the Fermi level. Momentum maps at these two binding energies are shown in Fig. 1.10 and compared to the calculated FTs of the HOMO and LUMO from an isolated 6P molecule (Figs. 1.10c and d). The main characteristics, maxima at $k_x^{\mathrm{HOMO}} \approx \pm 1.45\ \text{Å}^{-1}$ reflecting the spatial periodicity set